The published paper may be found at: https://doi.org/10.1115/1.4051989

For citation:
Kutkan, H., Amato, A., Campa, G., Ghirardo, G., Tay Wo Chong, L., and Æsøy, E. (October 20, 2021). "Modeling of Turbulent Premixed CH4/H2/Air Flames Including the Influence of Stretch and Heat Losses." ASME. J. Eng. Gas Turbines Power. January 2022; 144(1): 011020.

Modelling of Turbulent Premixed CH_4/H_2/Air Flames Including the Influence of Stretch and Heat Losses

Halit Kutkan, first author[1]
University of Genoa
16145 Genoa, Italy
halit.kutkan@edu.unige.it

Alberto Amato, second author
Ansaldo Energia S.p.A.
16152 Genoa, Italy
alberto.amato@ansaldoenergia.com

Giovanni Campa, third author
Ansaldo Energia S.p.A.
16152 Genoa, Italy
giovanni.campa@ansaldoenergia.com

Giulio Ghirardo, fourth author
Doodle AG
8021 Zürich, Switzerland
giulio.ghirardo@gmail.com

Luis Tay Wo Chong, fifth author
Ansaldo Energia Switzerland AG
5401 Baden, Switzerland
luis.taywochonghilares@ansaldoenergia.com

Eirik Æsøy, sixth author
Norwegian University of Science and Technology
NO-7491 Trondheim, Norway
eirik.asoy@ntnu.no

[1] Corresponding author: Halit Kutkan, halit.kutkan@edu.unige.it

ABSTRACT

This paper presents a RANS turbulent combustion model for CH_4/H_2/air mixtures which includes the effect of heat losses and flame stretch. This approach extends a previous model concept designed for methane/air mixtures and improves the prediction of flame stabilization when hydrogen is added to the fuel. Heat loss and stretch effects are modelled by tabulating the consumption speed of laminar counter flow flames in a fresh-to-burnt configuration with detailed chemistry at various heat loss and flame stretch values. These computed values are then introduced in the turbulent combustion model by means of a turbulent flame speed expression which is derived as a function of flame stretch, heat loss and H_2 addition. The model proposed in this paper is compared to existing models on experimental data of spherical expanding turbulent flame speeds. The performance of the model is further validated by comparing CFD predictions to experimental data of an atmospheric turbulent premixed bluff-body stabilized flame fed with CH_4/H_2/air mixtures ranging from pure methane to pure hydrogen.

1. INTRODUCTION

In view of the global efforts for the decarbonization of the power generation sector, in recent years there is an increased interest in the development of gas turbine engines able to introduce hydrogen blending into the normal natural gas fuel supply. Hydrogen is seen as a promising option to store excess energy produced from renewable sources, such as wind and solar. Gas turbine engines fed by hydrogen/natural gas could in the future complement the intermittent renewable power supply by working as back-up power during periods of scarce wind and daylight [1,2]. However, current lean-premixed combustor technologies are not yet able to handle reliably the full range of 0-100% hydrogen contents blended with natural gas. One challenge in the development of such systems is to control and predict how the flame stabilizes inside the combustor when

hydrogen, which has a higher reactivity than natural gas, is added to the fuel. Flame stabilization in lean-premixed combustors is commonly achieved by recirculating hot gases by means of bluff-bodies and swirlers. Depending on the interplay between hydrogen addition, heat losses and flame stretch in the hot gas recirculation zones, different flame stabilization shapes (such as M-flames, V-flames or detached flames) can be present in a combustor, as for example shown in [3] for a swirl stabilized flame and in [4] for a bluff-body stabilized flame. For CH_4/air flames, past studies [5–7] demonstrate that CFD RANS models can correctly predict flame stabilization in lean-premixed combustors by including the effect of stretch and heat losses in the turbulent combustion model. The objective of the present work is to include the effect of enhanced reactivity due to hydrogen addition into the modelling concept proposed in [5–7], which was previously not considered.

The rest of the paper is organized as follows. Section 2 describes laminar flame calculations in a canonical setup that shows the effect of stretch, heat loss and hydrogen addition on premixed flames. These calculations form the basis of the turbulent premixed combustion model described in section 3. The turbulent combustion model proposed in this paper is compared to both the previous model for CH_4/air [5] and another popular model for CH_4/H_2/air turbulent premixed flames [8]. Then, in section 4 the performance of these three turbulent combustion models is compared with turbulent flame speed data measured in spherically expanding turbulent flame experiments available in the open literature [9–12]. Finally, section 5 further compares the performance of the three turbulent combustion models by illustrating CFD RANS computations of an atmospheric

83 premixed turbulent bluff-body-stabilized configuration [4] which was fed with CH_4/H_2/air
84 mixtures ranging from pure methane to pure hydrogen.
85
86 **2. LAMINAR FLAME ANALYSIS**
87
88 As a first step, the influence of stretch and heat loss on a laminar flame is analyzed
89 numerically in an asymmetric "fresh-to-burnt" counter-flow configuration (see Fig. 1). The
90 calculations presented in this paper were performed using Cantera 2.3.0 [13] with the
91 GRI-Mech 3.0 [14] chemical mechanism. Past studies find that laminar flame speeds for
92 CH_4/H_2/air mixtures calculated with this mechanism are in reasonable agreement with
93 experimental data [15,16]. A multicomponent formulation is used to model transport
94 properties. In order to simulate different levels of heat loss from the flame, the
95 temperature of the unburnt mixture (T_u) is kept constant while the temperature of the
96 products (T_p) is gradually decreased starting from the adiabatic flame temperature (T_{ad}).
97 The effect of heat loss is parametrized defining a heat loss coefficient β as:

$$\beta = \frac{T_p - T_u}{T_{ad} - T_u} \quad (1)$$

98 Flame stretch, defined by the fractional rate of change of flame surface area, is
99 produced by the combination of strain and curvature. In this work, the influence of
100 curvature is considered small [17,18] and only the contribution from the strain is
101 considered. To simulate the effect of flow strain on the flame, the flow velocities of
102 reactants and products are increased gradually until either flame extinction occurs or a
103 maximum prescribed level of strain is reached. The momentum of reactants and products

is kept always equal to maintain the stagnation plane position approximately constant. The flame stretch κ considers only the effects from strain and is evaluated as the maximum velocity gradient at the unburnt side (Eq. (2)):

$$\kappa = max\left|-\frac{\partial u_x}{\partial x}\right| \quad (2)$$

Fig. 2 shows the computed effect of strain and heat losses on the laminar flame consumption speed S_c of an asymmetric counter-flow flame for different levels of hydrogen addition. The flame consumption speed is defined as:

$$S_c = \frac{1}{\rho_u \Delta H_c^o Y_f} \int_{-\infty}^{\infty} \dot{q}\, dx \quad (3)$$

where ΔH_c^o is the lower heating value of the combustion, ρ_u is the unburnt mixture density, Y_f is the mass fraction of the fuel in the reactants and $\dot{q}$ is the total heat release rate per unit volume.

Calculations show that at high values of stretch and heat losses a high decrement on the consumption speed is observed indicating strong levels of quenching [19]. Increasing hydrogen content decreases the sensitivity of consumption speed to flame stretch and heat losses. For the mixtures with H_2 addition (Fig. 2 (b) and (c)), flame stretch increases the consumption speed initially and then decreases. This trend is not observed on the pure CH_4 flames as S_c has a monotonic decrease with increasing flame stretch. The increment of S_c from low stretch values is attributed to the high diffusivity (Le number effect) of H_2, and this effect increases and becomes more remarkable with the increasing content of the hydrogen in the mixture [20].

For CFD simulations, look-up tables were created for the S_c consumption speeds of 5 different fuel mixtures under experimental conditions listed in Table 1. While forming the consumption speed S_c look-up tables, strain κ points were sampled from 0 to 30000 1/s, and β heat loss coefficient points were sampled from 1 to 0.4. For $\beta \leq 0.4$ flame quenching is observed for all the investigated conditions. Similar approach using look-up tables to introduce effects of stretch and heat loss was used in [21,22]. The concept to introduce effects of stretch and heat loss can be also applied to other models as for example in the FGM context as done by Klarmann et al. [21]. Laminar unstretched flame speed S_{L0} is calculated from Eq. (3) using Cantera "FreeFlame" module. S_{L0} is equivalent to $S_c(\kappa = 0, \beta = 1)$.

3. TURBULENT PREMIXED COMBUSTION MODEL

The Turbulent Flame Closure (TFC) combustion model [23] in the RANS framework involves the solutions of a transport equation for the density-weighted reaction progress variable $\tilde{c}$:

$$\frac{\partial(\bar{\rho}\tilde{c})}{\partial t} + \frac{\partial\left(\bar{\rho}\tilde{u}_j\tilde{c}\right)}{\partial x_j} = \frac{\partial}{\partial x_j}\left(\bar{\rho}\frac{\nu_t}{Sc_t}\frac{\partial\tilde{c}}{\partial x_j}\right) + \bar{\dot{\omega}} \tag{4}$$

where the reaction rate source term $\bar{\dot{\omega}}$ is modelled as:

$$\bar{\dot{\omega}} = \rho_u S_T |\nabla\tilde{c}| \tag{5}$$

The closure of this term requires a model for the turbulent flame speed S_T. TFC combustion models are relatively simple to implement, but their success in modelling flame propagation relies on the accuracy of the S_T expression. In the following, two

previously proposed models (Sec. 3.1 and 3.2) are presented and then the S_T model proposed in this paper for CH_4/H_2/air flames is described (Sec. 3.3).

3.1. Algebraic Flame Surface Wrinkling (AFSW) Model

In [24,25] a turbulent flame speed expression for CH_4/H_2/air flames was proposed building upon previous models for hydrocarbon/air flames:

$$S_T = S_{L0} + \frac{0.46}{e^{Le^*-1}} u'^{0.55} S_{L0}^{0.7} \nu^{-0.25} l_t^{0.25} \left(\frac{P}{1atm}\right)^{0.2} \quad (4)$$

where u' is turbulent velocity, S_{L0} is the unstretched laminar flame speed, ν is the laminar kinematic viscosity, l_t the turbulence length scale and P is the pressure. In Eq. (6), turbulent velocity u' and length scale l_t are calculated as indicated in the original references [24,25]:

$$u' = \sqrt{\frac{2}{3}k} \ , \ l_t = c_\mu^{3/4} \frac{k^{3/2}}{\varepsilon} \quad (5)$$

where k and ε refer to turbulence kinetic energy and dissipation rate, respectively, and $c_\mu = 0.09$. The "effective Lewis number" Le^* is introduced to model the effect of the different molecular diffusivity of hydrogen and methane on the turbulent flame speed [24,25]. It is well known that different fuel molecular diffusivities can affect burning rates up to very high turbulent intensities [26,27]. Le^* is defined as:

$$Le^* = \frac{\alpha}{x_{CH_4} D_{CH_4} + x_{H_2} D_{H_2}} \quad (6)$$

where α is the thermal diffusivity, x_{CH_4} and x_{H_2} are the volumetric fraction of methane and hydrogen in the fuel, respectively, while D_{CH_4} and D_{H_2} represent the binary molecular

mass diffusion coefficients with respect to inert N_2 gas of methane and hydrogen, respectively. The values of α, D_{CH_4} and D_{H_2} in Eq. (8) are evaluated at the temperature, pressure and composition of the reactants.

In [24] it is shown that a RANS TFC model coupled with Eq. (6) was able to fit experimental data of adiabatic turbulent Bunsen-type flames reasonably well up to 30-40% H_2 content (volumetric) in the fuel stream.

3.2. Extended TFC (ExtTFC) Model

For CH_4/air flames the following expression was proposed in [5]:

$$S_T = 0.52{u'}^{0.75} S_c^{0.5} \alpha_u^{-0.25} l_t^{\ 0.25} \tag{7}$$

where the turbulent velocity and length scale are calculated as:

$$u' = \sqrt{\frac{2}{3}k}\ ,\ \ l_t = 0.37\frac{{u'}^3}{\varepsilon} \tag{8}$$

Eq. (9) is the same as the classical Zimont turbulent flame speed expression [23,28,29], but in this formulation the unstretched adiabatic laminar flame speed S_{L0} is replaced by the stretched non-adiabatic laminar flame consumption speed S_c which is a function of stretch and heat losses $S_c = f(\kappa, \beta)$ and is computed from laminar 1D calculations as described in section 2. In RANS computations of turbulent flames, the values of κ and β necessary to evaluate S_c are calculated as explained next.

The heat loss coefficient β defined in Eq. (1) is calculated as in [7]:

$$\beta = 1 - \frac{h_u - \tilde{h}}{\tilde{c} Y_f \Delta H_c^0} \tag{9}$$

where h_u, Y_f and ΔH_c^0 are total unburnt enthalpy (sensible plus the standard formation enthalpy), fuel mixture fraction and lower heating value of the fuel, respectively. The averaged enthalpy $\tilde{h}$ is obtained by solving an averaged enthalpy transport equation for the turbulent flow.

To evaluate the flame stretch κ the following expression is used:

$$\kappa = \underbrace{\left(\delta_{ij} - \widetilde{n_i n_j}\right)\frac{\partial \widetilde{u_i}}{\partial x_j}}_{\kappa_{mean}} + \underbrace{\Gamma_K\left(\frac{u'}{S_{L0}}, \frac{L}{\delta_{L0}}\right)\frac{\varepsilon}{k}\left[\frac{1}{Le}\left(1.76 + \tanh(Le - 2)\right)\right]}_{\kappa_{turb}} \quad (10)$$

The term, κ_{mean}, is the stretch due to the mean flow. δ_{ij} is the Kronecker delta and the orientation factors $\widetilde{n_i n_j}$ are calculated as follows [30]:

$$\widetilde{n_i n_i} = \frac{\sum_{k \neq i} \widetilde{u'^2_k}}{4k} \quad , \quad \widetilde{n_i n_{j \neq i}} = \frac{\widetilde{u'_i u'_j}}{2k} \quad (11)$$

where $\widetilde{u'_i u'_j}$ are the averaged Reynolds stresses, and k is the turbulent kinetic energy. The term, κ_{turb}, models the average flame stretch due to turbulent eddies. The term Γ_K is the ITNFS (Intermittent Turbulence Net Flame Stretch) efficiency function and is calculated following [31,32]. The resulting turbulent flame stretch is computed by multiplying Γ_K by the inverse of the characteristic eddy time scale ε/k [33]. In this paper, improving upon the model used in [5–7], κ_{turb} contains also a term that depends on the Lewis number Le of the fuel. This term is proposed in [34] to better fit average turbulent flame stretch values computed from direct numerical simulations of CH_4/H_2/air and C_3H_8/H_2/air flames. For $Le = 1$ this term is equal to 1 thus recovering the κ_{turb} expression used [5–7] for CH_4/air flames. Following the notation of [31,34], in Eq. (12) the turbulent integral length scale L is computed as $L = u'^3/\varepsilon$, u' is calculated as in Eq. (10), the laminar

flame thickness δ_{L0} is calculated from the maximum temperature gradient of a 1D unstretched laminar flame $\delta_{L0} = (T_{ad} - T_u)/\max(dT/dx)$ and the Lewis number is calculated as $Le = x_{CH_4}\,\alpha/D_{CH_4} + x_{H_2}\,\alpha/D_{H_2}$, where the various terms are evaluated as in Eq. (8).

The performance of RANS TFC computations coupled with Eq. (9) is evaluated in [5] and it is shown that this model is able to predict cold wall quenching effects and the correct flame shape for CH_4/air turbulent flames in swirl stabilized combustors. Later this approach is also successfully extended to large eddy simulations (LES) [6], where it showed a good match between the calculated and measured flame response to acoustic oscillations.

3.3. Extended TFC for CH_4/H_2 Mixtures (ExtH_2TFC)

In the context of this study, the following turbulent flame speed expression for CH_4/H_2/air flames is proposed:

$$S_T = S_c + \frac{0.4}{\sqrt{Le^*}} u'^{0.8} S_c^{0.45} \alpha_u^{-0.25} l_t^{0.25} \qquad (12)$$

Eq. (14) draws upon the S_T expressions of Eq. (6) and (9) with the following similarities and differences.

First, in Eq. (14) the effective Lewis number Le^* is included to model the effect of hydrogen molecular diffusion on S_T, mimicking the approach that led to the development of Eq. (6). However, here S_T is considered that it varies proportionally to $Le^{*-0.5}$ and not e^{1-Le^*}. This different exponent was proposed in the recent study described in [11] where

it was found that $Le^{*-0.5}$ was able to best fit turbulent flame speed experimental data of pure hydrogen, propane and isooctane flames. Furthermore, Le^* in Eq. (14) is calculated as in Eq. (8) but the transport properties, α, D_{CH_4} and D_{H_2} are computed at the temperature corresponding to the location of maximum heat release rate in a 1D unstretched laminar flame. This different evaluation method of Le^* was proposed in [24] because the diffusivity of hydrogen in the reaction zone of the flame is considered more meaningful for the description of the interaction between flame molecular diffusion processes and turbulent eddies.

Second, the use of S_c instead of S_{L0} is retained from Eq. (9) to model stretch and heat loss effects. This is particularly important to reflect the quenching effects at the outer shear layer. The exponent of u' and S_c are adjusted compared to Eq. (9) primarily to achieve a better fit with the turbulent flame speed experimental data described in the next section. For the same reason the pre-factor value is changed to 0.4 compared to the original value 0.52 also to compensate for the fact that in Eq. (14) for the definition of u' and l_t Eq. (7) is used instead of Eq. (10). Note that the original exponents in the Zimont S_T expression (Eq. (9)) were derived by means of theoretical arguments based on the dimensional analysis of the propagation of 1D turbulent flame [28]. Here the small adjustment is reasonable because in S_c there is already a built in dependence on u' through the stretch factor κ which was not present in [28].

Third, compared to Eq. (9), in Eq. (14) the S_c term was added to S_T in order to recover the laminar flame propagation speed at $u' = 0$. In fact, for high hydrogen content S_c values can become a significant contribution to the turbulent flame propagation.

Finally, we remark that Eq. (14) in this paper is validated for lean and stoichiometric equivalence ratios under atmospheric pressure. The validity of this formulation for high pressure and rich mixture conditions will be subject of future studies. In particular, the inclusion of an explicit dependence of S_T on pressure as in Eq. (6) was not investigated.

4. TURBULENT FLAME SPEED RESULTS

In this section the performance of the S_T expressions of the AFSW, ExtTFC and ExtH_2TFC models is compared with the turbulent flame speeds values measured in the fan stirred bomb experiments of refs. [9–12]. In these experiments the flame is propagating in isotropic turbulence with zero mean velocity, which results in $\kappa_{mean} = 0$ and $\kappa = \kappa_{turb}$ in Eq. (12). It is also assumed that in these experiments heat losses are negligible (i.e. $\beta = 1$). The values of turbulent velocity u' and turbulent integral length scale L are taken as specified in the original references for each measurement and, the different definitions of turbulent length scale l_t in Eq. (7) and (10) are computed from the linear relation between L and l_t. The experimental turbulent flame data in [9–12] were all measured by reconstructing the average flame radius R_{sch} from Schlieren photography as it evolves in time. Since different references use different turbulent flame speed definitions, in this paper the turbulent flame speed data are always extracted from the following definition by manipulating the data of the original references:

$$S_{T,c=0.5} = \left(\frac{1}{1.11}\frac{\rho_b}{\rho_u}\right)\left(\frac{R_{c=0.1}}{R_{c=0.5}}\right)^2 \frac{dR_{sch}}{dt} \tag{13}$$

where dR_{sch}/dt is the time derivative of the mean flame radius, while ρ_b and ρ_u are the burnt and unburnt gas density, respectively. The factor $1/1.11$ is an empirical constant

proposed in [9] which is needed to convert the displacement speed dR_{sch}/dt measured from Schlieren photography to turbulent mass burning rate. Additionally, the coefficient $R_{c=0.1}/R_{c=0.5} = 1.4$ was suggested in [10] as a converting factor to obtain the turbulent flame speed at $\tilde{c} = 0.5$. For each experiment the average dR_{sch}/dt value in the interval $25\ mm < R_{sch} < 45\ mm$ and the repeated measurements at the same conditions were arithmetically averaged.

Fig. 3 and Fig. 4 show the comparison of the different turbulent flame speed expressions with experimental data. For the AFSW the agreement between the model and the data is good, except for the 80% H_2-20% CH_4 fuel mixture in Fig. 4. On the contrary, as expected, the ExtTFC model matches well the 100% CH_4 turbulent flame speed data but underpredicts them when H_2 is added to the fuel. The ExtH_2TFC model instead matches well all the experimental data investigated in this paper. Especially the $Le^{*-0.5}$ factor in the ExtH_2TFC model is fundamental to correctly match the turbulent flame speed experimental data in adiabatic isotropic turbulence conditions. In the next section, the performance of the models is further tested in 3D CFD simulations.

5. CFD MODELLING

In this section, the experimental setup, numerical details, cold flow and reacting CFD results are presented.

5.1. Experimental Setup

Fig. 5 shows the atmospheric rig experimental setup. Cylindrical combustion chamber has the inner diameter of d_q = 44 mm with 3 mm thick quartz walls, and has the length of L_q = 75 mm. The combustor has been operated with 5 different mixtures of CH_4/H_2/air premixed gas, from 0% H_2 to 100% H_2 content in the fuel. The mixture properties and inlet conditions are presented in the Table 1. The flow rates are adjusted by Alicat mass flow controllers and the bulk flow velocity is calculated from the volumetric flow rate. Air and fuel are mixed a meter before the plenum entrance in order to provide the fully premixed condition. The mixture enters a pipe section with d_p = 19 mm. The flame is stabilized by a bluff-body (d_b = 13 mm) producing a blockage ratio of 47% and supported by a center rod (d_r = 5 mm).

The rod is held by 3 grub screws (d_g = 4 mm) at 45 mm upstream from the dump plane as sketched in Fig. 5. PIV measurements of the cold flow were carried out using Phantom V2012 (LaVision IRO) camera and a Photonics DM100 dual head laser, by ensemble averaging of 5000 vector fields. OH^* Chemiluminescence imaging was captured using the same camera setup with a Cerco 2178 UV 100F/2.8 lens equipped with 310 ± 10-nanometer band pass filter and the planar view was obtained using a 3 point Abel deconvolution. Further information on the experimental set-up are available in [4].

5.2. Numerical Methods and Boundary Conditions

CFD studies were carried out in Ansys Fluent 2019 R3 on the 3D geometry. The combustion chamber length has been doubled in the computational domain to increase the distance between the outlet boundary condition and the flame in order to provide flow continuity.

Fig. 6 shows the geometry dimensions and boundary names of the computational domain. Table 2 lists the implemented boundary conditions. The mesh was created using BetaCAE ANSA 20 software, having around 5 million cells in total and its section is shown in Fig. 7. The average y^+ value in the domain is below 2 ($y^+ \leq 2$) having $y^+ \approx 3$ in the inlet pipe section and $y^+ \leq 1$ in the combustion chamber section.

A solid bluff-body zone (CZC 2 in Table 2) is included with conjugate heat transfer calculations (BC 6 in Fig. 6). Reynolds stress (RSM) and k-ε realizable turbulence models with the Non-equilibrium wall function (NEWF) were compared with experiments in cold flow simulations. RSM model was selected for the reacting flow calculations (see section **Error! Reference source not found.**). The coupled scheme was used for pressure-velocity coupling. For spatial discretization, second order upwind was selected for Reynolds stresses, and the QUICK scheme was selected for all other equations. Calculations and experiments have been performed at atmospheric pressure. Mixture thermal conductivities and viscosities were calculated across the flame in Cantera for all fuel blends and introduced as temperature dependent polynomial coefficients in the CFD solver.

Bluff-body has been modelled as solid cell zone from z = 0 m to z = -0.035 m where z = 0 m is at the dump plane in Fig. 5 and 6. The combustion chamber back and side walls (BC 7 and 8 in Table 2) were modelled as shell conduction walls with thickness of 0.01 m and 0.003 m, respectively. Inconel material properties have been assigned to the bluff-body solid cell zone and combustion chamber back wall (CZC 2 and BC 7) and Quartz material properties have been assigned to the combustion chamber side walls (BC 8). Solid cell zone and wall thermal conductivities and specific heats were introduced as temperature dependent polynomials and obtained from [35,36] for Quartz and from [37] for Inconel.

5.3. Cold Flow Results

Reynolds stress (RSM) and k-ε realizable turbulence models were compared with cold flow PIV experiments in terms of z (axial) and x-velocity at different axial locations (z = 0.002 m, and z = 0.011 m). In Fig. 8, RSM model shows a better agreement with experiments than k-ε realizable model on both velocity components. Similar agreement was seen at other plane locations. Based on this, the RSM was selected as turbulence model of the reacting flow calculations.

5.4. Reacting Flow Results

The progress variable $\tilde{c}$ equation was solved using the non-adiabatic partially premixed combustion setup with chemical equilibrium chemistry model. Since the cases are perfectly premixed, equations of mixture fraction and its variance were disabled in the solution process. The combustion models were introduced via user defined functions (UDFs). The 3 turbulent flame speed approaches indicated in section 3 were evaluated. Look-up consumption speed tables ($S_c = f(\kappa, \beta)$) were calculated for the 5 different mixtures in Table 1. These tabulations were used for the ExtTFC and ExtH_2TFC models. Both extended models were evaluated using the same definition of stretch as in Eq. (12) which includes Le number effects. Keeping the same definition of stretch in both models allows a direct comparison of the turbulent flame speed definitions.

To take into account heat transfer effects, the combustor back and side walls (BC 7 and BC 8) were simulated considering heat transfer coefficient values indicated in Table 2. For the back wall, Yang's natural convection relation [38] was used. For the side wall, there is uncertainty on the induced velocity affecting the surface, as the experimental setup was placed under a big extracting flow diffuser for ventilation purposes. Wall temperature measurements in the evaluated experimental setup were not carried out. Nevertheless, to estimate the average values on the combustor side wall, temperature measurements taken for a similar setup (square combustion chamber operated with an ethylene flame) was used. For these measurements, the average temperature was in the range of 593 K – 833 K (at different locations from z = 0.01 m to z = 0.03 m) on the outside

surface of the combustor wall. To find a proper HTC for the side surface, a parametric study was conducted (not presented in the paper) by assigning different HTCs. HTC = 150 W/m^2K produced reasonable agreement on wall temperatures and flame shapes, as discussed in more detail at the end of this section.

In Fig. 10, heat release rate contours from the 3 different turbulent flame speed models are compared with the Abel deconvoluted OH^* chemiluminescence images from experiments. Heat release rate is computed as:

$$\mathrm{HRR} = \rho Y_f \Delta H_c^o \mathrm{PFR} \tag{14}$$

where ρ is the local density, PFR is the product formation rate, Y_f is the mixture fraction (which is constant along the whole domain in these fully premixed cases), and ΔH_c^o is the lower heating value of the fuel blends. For 0% H_2 (first row of Fig. 10), the ExtTFC and ExtH_2TFC models can correctly capture the mean flame shape producing a V-flame (stabilization mainly in inner shear layer) as in the experiment due to quenching effects in the outer shear layer. Flame stretch combined with heat losses are present in the outer shear layer (see Fig. 10 (b) and (c)), inducing quenching effects. The AFSW model produced the M-flame shape (strong reaction in the inner and outer shear layers) even under non-adiabatic conditions. The quenching in the outer layer seen in experiments is not captured (see Fig. 10 (a)) because the AFSW model does not consider the combined quenching effect of stretch and heat losses. The angle (with respect to the axial axis) of the inner flame with AFSW model is smaller than in experiments and extended models. Axial velocity contours in Fig. 9 show strong variations in the flow field between the M-

385 flame with AFSW model and the V-flame with ExtH_2TFC model. This indicates that the
386 prediction of flame topology has a strong impact on the flow field prediction.

387 The normalized axial heat release distribution is shown in the right column of Fig. 10
388 (normalized considering that the area of the distribution should be same for all cases as
389 the same amount of heat release is produced in experiments and simulations). The AFSW
390 model shows high values close to the dump plane producing a shorter flame than
391 experiments and extended models. Extended models show a better agreement to
392 experiments due to the similar flame shape. Results with 0% H_2 using the ExtTFC and
393 ExtH_2TFC models are similar as Lewis number is close to 1.

394 The impact of H_2 addition into the mixture is shown in Fig. 10. The 100% H_2 case has
395 higher inlet velocity and leaner mixture than the other cases (Table 1). Reactivity and
396 turbulent flame speed increase with H_2 addition, producing a decrease in flame length
397 and a change in flame topology after a certain % of H_2 content. In experiments, flame
398 stabilization in the outer shear layer starts to develop with 25.2% H_2, leading to M-flame
399 with 56.6% H_2. This transition effect is also captured by the ExtTFC and ExtH_2TFC models
400 (see the second row of Fig. 10 (b) and (c)). Calculations with AFSW model show the M-
401 flame shape for all H_2 contents with similar heat release intensity in both inner and outer
402 layers (Fig. 10 (a)). M-flames with extended models show a lower reaction in the outer
403 flame compared to the inner flame due to quenching effects.

404 Comparing extended models with experiments (Fig. 10 (b), (c) and (d)), the heat
405 release contours with the ExtH_2TFC model show good agreement in the flame shape for
406 all the H_2 contents. For cases with $H_2 > 50\%$, both extended models (see Fig. 10 (b) and

407 (c)) overpredict the flame quenching in the outer shear layer region close to the dump
408 plane which is highly affected by heat losses. Experiments show certain level of reaction
409 on that area. As shown in Fig. 11 (a), quenching occurs with $\beta \leq 0.5$, producing
410 overprediction of quenching on that region. Further developments are ongoing to
411 improve this prediction.

412 In addition, the ExtTFC model for the 56.6%, 67% and 100% H_2 cases show that, the
413 model predicts the same flame length for all three cases (see red lines belonging 56.6%,
414 67% and 100% H_2 cases in Fig. 10 (e), all three reach to zero intensity at $z = 0.05\ m$) while
415 both AFSW and ExtH_2TFC models predict decreasing flame lengths as H_2 percentage is
416 increasing due to the inclusion of the Le^* number term in the expressions. The ExtH_2TFC
417 model has an improvement compared to the AFSW and ExtTFC models as it includes
418 together the quenching effects due to stretch and heat losses and the increase in flame
419 reactivity due to Lewis number effects by H_2 addition.

420 With 100% H_2, the AFSW model shows a longer flame than experiments and extended
421 models, which is opposite to all other %H_2 cases shown in the results. The reason of this
422 low reactivity is associated with the fact that with high H_2 content, the consumption speed
423 S_c increases with stretch until a certain level and then decreases as seen in Fig. 11 (a).
424 These values even under heat loss effects are higher than the unstretched adiabatic
425 laminar flame speed S_{L0} (Fig. 11 (a) and (b)), leading to lower laminar flame speed values
426 in AFSW model than with extended models. The AFSW 100% H_2 case is longer than the
427 AFSW 67% H_2 case because it has a lower equivalence ratio with higher inlet velocity
428 (Table 1).

The impact of H_2 addition on stretch and heat losses is shown in Fig. 12 with a comparison of the cases with 0% H_2 and 56.6% H_2. Total stretch values are higher with H_2 addition (Fig. 12 (a)) as the Le number term in Eq. (12) produces an increase in the efficiency function, and κ_{mean} also increases in some regions due to the different flow and flame shapes. Similarly, different flow and flame structures affect heat losses too (Fig. 12 (b)).

For improvements in the model, it is observed that close to the dump plane (z = 0 in Fig. 10 (e) column, Axial HRR distribution plots) there are stronger heat release values in CFD models than experiments and that the flame brush from current RANS calculations is thinner than the one in experiments. As mentioned previously, ongoing work is in progress to improve the model considering the mentioned points.

Finally, the influence of uncertainty in the thermal boundary conditions in the combustor side wall was analyzed evaluating different HTC values. While HTC = 70-150 W/m^{2}K were producing flame shapes similar to the experiment for 0% H_2 case, for the 25.2% H_2 case different HTCs produced different flame shapes. As seen in the experiments (see Fig. 10 (d)), the case with 25.2% H_2 is a transition between the V-flame with 0% H_2 and the M-flame with 56.6% H_2. A reduction of the HTC to the range of 70-100 W/m^{2}K led to a marked increase of the reaction in the outer shear layer for the 25.2% H_2 case leading to a flame shape close to the M-flame seen for the case with 56.6% H_2. HTC = 150 W/m^{2}K provided the correct flame shape for all cases. Values of HTCs higher than 150 W/m^{2}K were not evaluated, since that value produced reasonable agreement on both wall temperatures and flame shapes with the ExtH_2TFC model.

6. CONCLUSION

A new turbulent flame speed correlation is proposed for CH_4/H_2/air mixtures that accounts for flame stretch, heat losses and effective Lewis number. It is derived based on two other turbulent flame speed approaches and calibrated against atmospheric lean and stoichiometric CH_4/H_2/air mixtures in spherical expanding turbulent flame experiments available in the literature, and further implemented in CFD RANS calculations.

Simulations are validated with atmospheric bluff-body stabilized CH_4/H_2/air turbulent premixed flame experiments from pure methane to pure hydrogen under lean mixture conditions. The proposed model is compared with two other combustion models and good agreement with experiments is obtained, presenting improvements with respect to existing state of the art models. Introduction of Lewis number effects are important for prediction of flame length especially at high H_2 contents in the mixture. The model predicts the correct flame stabilization topology attributed to the quenching effects produced by the combined effects of flame stretch and heat losses.

As further steps, extension of the model validation range to high pressure and rich conditions will be investigated. The use of a more recent chemical mechanisms as Aramco-Mech 1.3 [39], implementation of model improvements for a better prediction in RANS of the flame brush and reactions close to the anchoring location, and turbulent Schmidt number dependency in the model are also planned. Furthermore, the extension of the model to LES, similar to what done for CH_4/air mixture in ref. [6] may also be subject of study.

All these improvements look forward to improving the prediction of the flame shape and spatial distribution of heat release rate in order to better predict the flame dynamic response (flame transfer function) in turbulent flames with H_2 content.

ACKNOWLEDGMENT

This work is part of the Marie Skłodowska-Curie Initial Training Network Pollution Know-How and Abatement (POLKA). The authors gratefully acknowledge the financial support from the European Commission under call H2020-MSCA-ITN-2018 (project number: 813367).

FUNDING

Pollution Know-How and Abatement (POLKA) project is funded by the European Commission under call H2020-MSCA-ITN-2018 (project number: 813367).

NOMENCLATURE

Subscripts

u	unburnt mixture (i.e. reactants)
p	burnt mixture (i.e. products)
t	turbulent
ad	adiabatic

Superscripts

$'$	turbulent fluctuation
$\bar{}$	Reynolds averaged
$\tilde{}$	Favre averaged (density weighted Reynolds averaging)

Scripts

α	thermal diffusivity
β	heat loss coefficient
Γ_K	ITNFS efficiency function
δ_{L0}	Laminar unstretched adiabatic flame thickness
ε	turbulence dissipation rate
κ	flame stretch
ν	kinematic viscosity
$\dot{q}$	total heat release rate per volume

ρ	density
Φ	equivalence ratio
$\dot{\omega}$	reaction rate
c	progress variable (0 in the reactants, 1 in the products)
D	diffusion coefficient
h	enthalpy
k	turbulence kinetic energy
l	turbulent length scale
L	turbulent integral length scale
P	pressure
T	temperature
u	velocity
x	volumetric (or molar) fraction
HTC	heat transfer coefficient
Δh_{loss}	total enthalpy loss (i.e. heat loss)
ΔH_c^o	lower heating value
Le^*	effective Lewis number
Le	Lewis number

PFR	product formation rate
S_c	laminar flame consumption speed
Sc_t	turbulent Schmidt number
S_{L0}	laminar unstretched adiabatic flame speed
S_T	turbulent flame speed

496
497

REFERENCES

[1] ETN Global. "Hydrogen Gas Turbines: The Path Towards a Zero-Carbon Gas Turbine." www.etn.global/ETN-brochure (2020).

[2] Ciani, A., Tay-Wo-Chong, L., Amato, A., Bertolotto, E. and Spataro, G. "Hydrogen Blending into Ansaldo Energia AE94.3A Gas Turbine: High Pressure Tests, Field Experience and Modelling Considerations." *Proceedings of the ASME Turbo Expo 2021.* GT2021-58650. Virtual Online, June 7-11, 2021.

[3] Guiberti, T. F., Durox, D., Scouflaire, P. and Schuller, T. "Impact of heat loss and hydrogen enrichment on the shape of confined swirling flames." *Proc. Combust. Inst.* Vol. 35 Issue 2 (2015): pp. 1385–1392.
DOI: http://dx.doi.org/10.1016/j.proci.2014.06.016

[4] Æsøy, E., Aguilar, J. G., Wiseman, S., Bothien, M. R., Worth, N. A. and Dawson, J. R., "Scaling and prediction of transfer functions in lean premixed H2/CH4-flames". *Combust. Flame* Vol. 215 (2020): pp. 269–282.
DOI: https://doi.org/10.1016/j.combustflame.2020.01.045

[5] Tay Wo Chong, L., Komarek, T., Zellhuber, M., Lenz, J., Hirsch, C. and Polifke, W. "Influence of Strain and Heat loss on Flame Stabilization in a Non-Adiabatic Combustor." *Proceedings of the 4th European Combustion Meeting.* Vienna, AT, April 14-17, 2009.

[6] Tay Wo Chong, L., Scarpato, A. and Polifke, W. "LES Combustion Model With Stretch and Heat Loss Effects for Prediction of Premix Flame Characteristics and Dynamics." *Proceedings of ASME Turbo Expo 2017.* GT2017-63357, V04AT04A029. Charlotte, NC, USA, June 26-30, 2017.
DOI: https://doi.org/10.1115/GT2017-63357

[7] Tay Wo Chong, L., Zellhuber, M., Komarek, T., Im, H. G. and Polifke, W. "Combined Influence of Strain and Heat Loss on Turbulent Premixed Flame Stabilization." *Flow, Turbul. Combust.* Vol. 97 No. 1, (2016): pp. 263–294.
DOI: https://doi.org/10.1007/s10494-015-9679-0

[8] Muppala, S. P. R., Aluri, N. K., Dinkelacker, F. and Leipertz, A. "Development of an algebraic reaction rate closure for the numerical calculation of turbulent premixed methane, ethylene, and propane/air flames for pressures up to 1.0 MPa." *Combust. Flame* Vol. 140 Issue 4 (2005): pp. 257–266.
DOI: https://doi.org/10.1016/j.combustflame.2004.11.005

[9] Fairweather, M., Ormsby, M. P., Sheppard, C. G. W. and Woolley, R. "Turbulent burning rates of methane and methane-hydrogen mixtures." *Combust. Flame* Vol. 156 Issue 4 (2009): pp. 780–790.

DOI: https://doi.org/10.1016/j.combustflame.2009.02.001

[10] Jiang, L. J., Shy, S. S., Li, W. Y., Huang, H. M. and Nguyen, M. T. "High-temperature, high-pressure burning velocities of expanding turbulent premixed flames and their comparison with Bunsen-type flames." *Combust. Flame* Vol. 172 (2016): pp. 173–182.
DOI: https://doi.org/10.1016/j.combustflame.2016.07.021

[11] Nguyen, M. T., Yu, D. W. and Shy, S. S. "General correlations of high pressure turbulent burning velocities with the consideration of Lewis number effect." *Proc. Combust. Inst.* Vol. 37 Issue 2 (2019): pp. 2391–2398.
DOI: https://doi.org/10.1016/j.proci.2018.08.049

[12] Cai, X., Wang, J., Bian, Z., Zhao, H., Zhang, M. and Huang, Z. "Self-similar propagation and turbulent burning velocity of CH4/H2/air expanding flames: Effect of Lewis number." *Combust. Flame* Vol. 212 (2020): pp. 1–12.
DOI: https://doi.org/10.1016/j.combustflame.2019.10.019

[13] Goodwin, D. G., Speth, R. L., Moffat, H. K. and Weber, B. W. "Cantera: An object-oriented software toolkit for chemical kinetics, thermodynamics, and transport processes." 2017. Version 2.3.0.
https://www.cantera.org

[14] Smith, G. P., Golden, D. M., Frenklach, M., Moriarty, N. W., Eiteneer, B., Goldenberg, M., Bowman, C. T., Hanson, R. K., Song, S., Gardiner, W. C., Lissianski, V. V. and Qin, Z. "GRI-Mech 3.0"
http://www.me.berkeley.edu/gri_mech/

[15] Donohoe, N., Heufer, A., Metcalfe W. K., Curran, H. J., Davis, M. L., Mathieu, O., Plichta, D., Morones, A., Petersen, E. L. and Guthe, F. "Ignition delay times, laminar flame speeds, and mechanism validation for natural gas/hydrogen blends at elevated pressures." *Combust. Flame* Vol. 161 Issue 6 (2014): pp. 1432–1443.
DOI: https://doi.org/10.1016/j.combustflame.2013.12.005

[16] Ji, C., Wang, D., Yang, J. and Wang, S. "A comprehensive study of light hydrocarbon mechanisms performance in predicting methane/hydrogen/air laminar burning velocities." *Int. J. Hydrogen Energy* Vol. 42 Issue 27 (2017): pp. 17260–17274.
DOI: https://doi.org/10.1016/j.ijhydene.2017.05.203

[17] Mantel, T. and Samaniego, J. M. "Fundamental mechanisms in premixed turbulent flame propagation via vortex-flame interactions Part II: numerical simulation." *Combust. Flame* Vol. 118 Issue 4 (1999): pp. 557–582.
DOI: https://doi.org/10.1016/S0010-2180(99)00019-X

[18] Bradley, D., Gaskell, P. H., Sedaghat, A. and Gu, X. J. "Generation of PDFS for flame curvature and for flame stretch rate in premixed turbulent combustion." *Combust. Flame* Vol. 135 Issue 4 (2003): pp. 503–523.
DOI: https://doi.org/10.1016/S0010-2180(03)00181-0

[19] Mastorakos, E., Taylor, A. M. K. P. and Whitelaw, J. H. "Extinction of turbulent counterflow flames with reactants diluted by hot products." *Combust. Flame* Vol. 102 Issues 1-2 (1995): pp. 101–114.
DOI: https://doi.org/10.1016/0010-2180(94)00252-N

[20] Law, C. K. *Combustion Physics.* Cambridge University Press, Cambridge (2006).

[21] Klarmann, N., Sattelmayer, T., Geng, W., Zoller, B. T. and Magni, F. "Impact of flame stretch and heat loss on heat release distributions in gas turbine combustors: Model comparison and validation." in *Proceedings of the ASME Turbo Expo 2016*. GT2016-57625 V04BT04A031. Seoul, South Korea, June 13–17, 2016.
DOI: https://doi.org/10.1115/GT2016-57625

[22] Nassini, P. C., Pampaloni, D. and Andreini, A. "Inclusion of flame stretch and heat loss in LES combustion model." *AIP Conf. Proc.* Vol. 2191 Issue 1 (2019).
DOI: https://doi.org/10.1063/1.5138852

[23] Zimont, V., Polifke, W., Bettelini, M. and Weisenstein, W. "An efficient computational model for premixed turbulent combustion at high reynolds numbers based on a turbulent flame speed closure." *J. Eng. Gas Turbines Power* Vol. 120 Issue 3 (1997): pp. 526-532.
DOI: https://doi.org/10.1115/1.2818178

[24] Dinkelacker, F., Manickam, B. and Muppala, S. P. R. "Modelling and simulation of lean premixed turbulent methane/hydrogen/air flames with an effective Lewis number approach." *Combust. Flame* Vol. 158 Issue 9 (2011): pp. 1742–1749.
DOI: https://doi.org/10.1016/j.combustflame.2010.12.003

[25] Muppala, S. P. R., Manickam, B. and Dinkelacker, F. "A comparative study of different reaction models for turbulent methane/hydrogen/air combustion." *J. Therm. Eng.* Vol. 1 No. 5 (2015): pp. 367–380.
DOI: 10.18186/jte.60394

[26] Lipatnikov, A. N. and Chomiak, J. "Turbulent flame speed and thickness: phenomenology, evaluation, and application in multi-dimensional simulations." *Prog. Energy Combust. Sci.* Vol. 28 Issue 1 (2002): pp. 1–74.
DOI: https://doi.org/10.1016/S0360-1285(01)00007-7

[27] Bell, J. B., Cheng, R. K., Day, M. S. and Shepherd, I. G. "Numerical simulation of Lewis number effects on lean premixed turbulent flames." *Proc. Combust. Inst.* Vol. 31 Issue 1 (2007): pp. 1309–1317.
DOI: https://doi.org/10.1016/j.proci.2006.07.216

[28] Zimont, V. L. "Theory of Turbulent Combustion of a Homogeneous Fuel Mixture at High Reynolds Numbers." *Combust. Explos. Shock Waves* Vol. 15 (1979): pp. 305–311.
DOI: https://doi.org/10.1007/BF00785062

[29] Zimont, V. L. "Gas premixed combustion at high turbulence. Turbulent Flame closure combustion model." *Exp. Therm. Fluid Sci.* Vol. 21 Issues 1-3 (2000): pp. 179–186.
DOI: https://doi.org/10.1016/S0894-1777(99)00069-2

[30] Veynante, D., Piana, J., Duclos, J. M. and Martel, C. "Experimental analysis of flame surface density models for premixed turbulent combustion." *Symposium (International) on Combustion* Vol. 26 Issue 1 (1996): pp. 413–420.
DOI: https://doi.org/10.1016/S0082-0784(96)80243-8

[31] Meneveau, C. and Poinsot, T. "Stretching and quenching of flamelets in premixed turbulent combustion." *Combust. Flame* Vol. 86 Issue 4 (1991): pp. 311–332.
DOI: https://doi.org/10.1016/0010-2180(91)90126-V

[32] Poinsot, T. and Veynante, D. *Theoretical and Numerical Combustion.* 3rd edition by Poinsot and Veynante, Bordeaux (2012).

[33] Duclos, J. M., Veynante, D. and Poinsot, T. "A comparison of flamelet models for premixed turbulent combustion." *Combust. Flame* Vol. 95 Issues 1-2 (1993): pp. 101–117.
DOI: https://doi.org/10.1016/0010-2180(93)90055-8

[34] Bougrine, S., Richard, S., Colin, O. and Veynante, D. "Fuel composition effects on flame stretch in turbulent premixed combustion: Numerical analysis of flame-vortex interaction and formulation of a new efficiency function." *Flow, Turbul. Combust.* Vol. 93 (2014): pp. 251–289.
DOI: https://doi.org/10.1007/s10494-014-9546-4

[35] Sergeev, O. A., Shashkov, A. G. and Umanskii, A. S. "Thermophysical Properties of Quartz Glass." *Journal of Engineering Physics* Vol. 43 (1982): pp. 1375–1383.
DOI: https://doi.org/10.1007/BF00824797

[36] Hemingway, B. S. "Quartz: heat capacities from 340 to 1000 K and revised values for the thermodynamic properties." *Am. Mineral.* Vol. 72 No. 3-4 (1987): pp. 273–279.

[37] Agazhanov, A. S., Samoshkin, D. A. and Kozlovskii, Y. M. "Thermophysical properties of Inconel 718 alloy." *J. Phys. Conf. Ser.* Vol. 1382 (2019): pp. 012175.

DOI: 10.1088/1742-6596/1382/1/012175

[38] Popiel, C. O. "Free convection heat transfer from vertical slender cylinders: A review." *Heat Transf. Eng.* Vol. 29 No.6 (2008): pp. 521–536.
DOI: https://doi.org/10.1080/01457630801891557

[39] Metcalfe, W. K., Burke, S. M., Ahmed, S. S. and Curran, H. J. "A hierarchical and comparative kinetic modeling study of C1 - C2 hydrocarbon and oxygenated fuels." *Int. J. Chem. Kinet.* Vol. 45 (2013): pp. 638–675.
DOI: https://doi.org/10.1002/kin.20802

684 **Table Captions List**

685

Table 1 Operating conditions in terms of thermal power, volume fraction of H_2 in the fuel, equivalence ratio and inlet bulk velocity.

Table 2 Boundary conditions for the domain in Fig. 6

686

687

688 Table 1 Operating conditions in terms of thermal power, volume fraction of H_2 in the
689 fuel, equivalence ratio and inlet bulk velocity.
690

$P\ [kW]$	$V_{H_2}\ [\%]$	Φ [-]	$u_{inlet}\ [m/s]$
7	0	0.7	11.8
7	25.2	0.7	11.8
7	56.6	0.7	11.5
7	67	0.7	11.4
7	100	0.4	17.1

691
692

693 Table 2 Boundary conditions for the domain in Fig. 6
694

Boundary	Boundary condition
BC1	Velocity inlet BC, $I = 5\%$, $d_{hyd} = 0.014\ m$, $T = 296\ K$
BC2	Pressure outlet (atmospheric pressure)
BC3, BC4, BC5	Wall, zero heat flux
BC6	Thermal coupled wall, Inconel material
BC7	Wall, Inconel with shell conduction, $\mathrm{HTC} = 8.6\ W/m^2K$, $t = 10\ mm$, $T_\infty = 296\ K$
BC8	Wall, Quartz wall shell conduction, $\mathrm{HTC} = 150\ W/m^2K$, $t = 3\ mm$, $T_\infty = 296\ K$
CZC1	Fluid zone
CZC2	Solid zone, Inconel material

695
696
697

698 **Figure Captions List**
699

Fig. 1 Fresh-to-burnt counter flow flame configuration.

Fig. 2 Laminar consumption speeds $S_c(\kappa, \beta)$ as function of flame stretch κ and heat loss coefficient β for (a) 0% H_2 + 100% CH_4, (b) 50% H_2 + 50% CH_4 and (c) 100% H_2 + 0% CH_4 under $P = 1\ atm$, $T_u = 300\ K$, $\Phi = 0.6$ conditions. Evaluated with GRI-mech 3.0 in cantera 2.3.0 with fresh-to-burnt counter flow flame configuration.

Fig. 3 Turbulent flame speed S_T vs turbulence velocity u' under atmospheric pressure with different H_2 contents in CH_4 (0%, 10%, 20% and 50% volumetric): symbols refer to the experimental data of Fairweather et al. [9], lines refer to the S_T models described in section 3.

Fig. 4 Turbulent flame speed S_T vs turbulence velocity u' under atmospheric pressure with different H_2 contents in CH_4 (0%, 80% and 100% volumetric): symbols refer to the experimental data of Jiang et al. [10], Nguyen et al. [11] and Cai et al. [12], lines refer to the S_T models described in section 3.

Fig. 5 Single sector atmospheric test rig schematical view.

Fig. 6 Measurements (in mm) of burner CAD geometry and boundary names of computational domain.

Fig. 7 Computational grid section view.

Fig. 8 Cold-flow z (axial) and x (transversal) velocities at different axial positions with different turbulence models ($u_{inlet} = 11.8\ m/s$).

Fig. 9 Axial velocity for (a) AFSW and (b) ExtH_2TFC with 0% H_2 reacting flow.

Fig. 10 Heat release rate distributions from 3 different turbulent flame speed models: (a) AFSW, (b) ExtTFC, (c) ExtH_2TFC and (d) Abel deconvoluted OH^* chemiluminescence images from experiments. (e) Normalized axial heat release distributions are shown in the right column. values are normalized with the maximum local intensity.

Fig. 11 (a) Laminar consumption speed $S_c(\kappa, \beta)$ as function of flame stretch κ and heat loss coefficient β, (b) ratio of consumption speed $S_c(\kappa, \beta)$ to unstretched laminar flame speed S_{L0} contours (from ExtH_2TFC model) for 100% H_2 + 0% CH_4 CFD case.

Fig. 12 (a) Total stretch κ, (b) heat loss coefficient β contours from the case with 0% and 56.6% H_2 contents (obtained with ExtH_2TFC model).

700
701

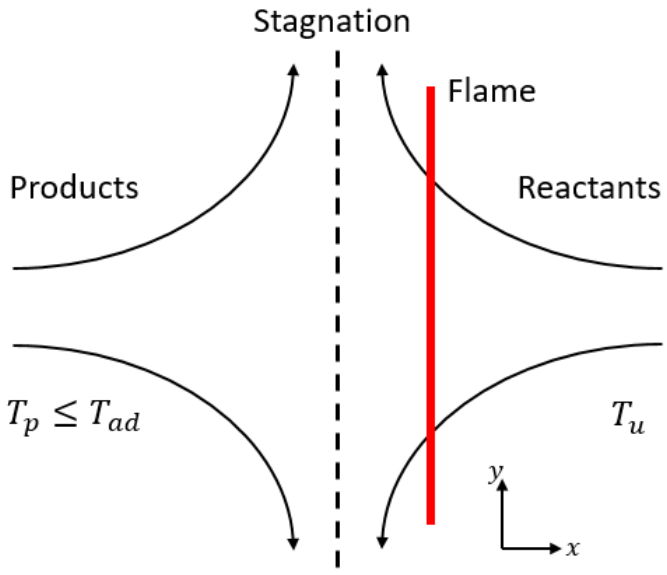

Fig. 1 Fresh-to-burnt counter flow flame configuration.

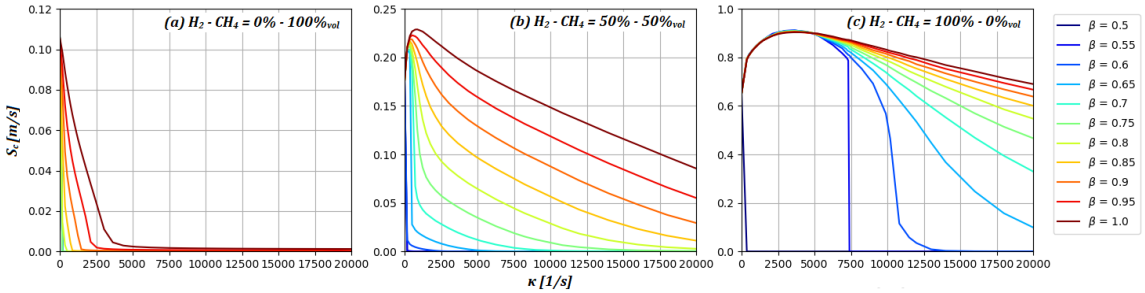

Fig. 2 Laminar consumption speeds $S_c(\kappa, \beta)$ as function of flame stretch κ and heat loss coefficient β for (a) 0% H_2 + 100% CH_4, (b) 50% H_2 + 50% CH_4 and (c) 100% H_2 + 0% CH_4 under $P = 1\ atm,\ T_u = 300\ K,\ \Phi = 0.6$ conditions. Evaluated with GRI-mech 3.0 in cantera 2.3.0 with fresh-to-burnt counter flow flame configuration.

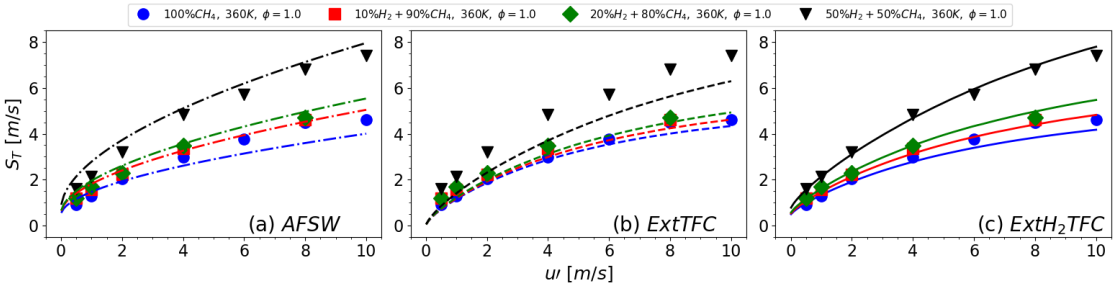

Fig. 3 Turbulent flame speed S_T vs turbulence velocity u' under atmospheric pressure with different H_2 contents in CH_4 (0%, 10%, 20% and 50% volumetric): symbols refer to the experimental data of Fairweather et al. [9], lines refer to the S_T models described in section 3.

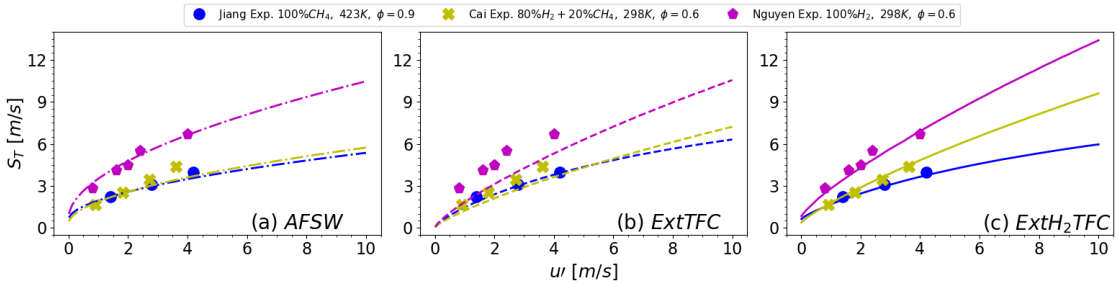

Fig. 4 Turbulent flame speed S_T vs turbulence velocity u' under atmospheric pressure with different H_2 contents in CH_4 (0%, 80% and 100% volumetric): symbols refer to the experimental data of Jiang et al. [10], Nguyen et al. [11] and Cai et al. [12], lines refer to the S_T models described in section 3.

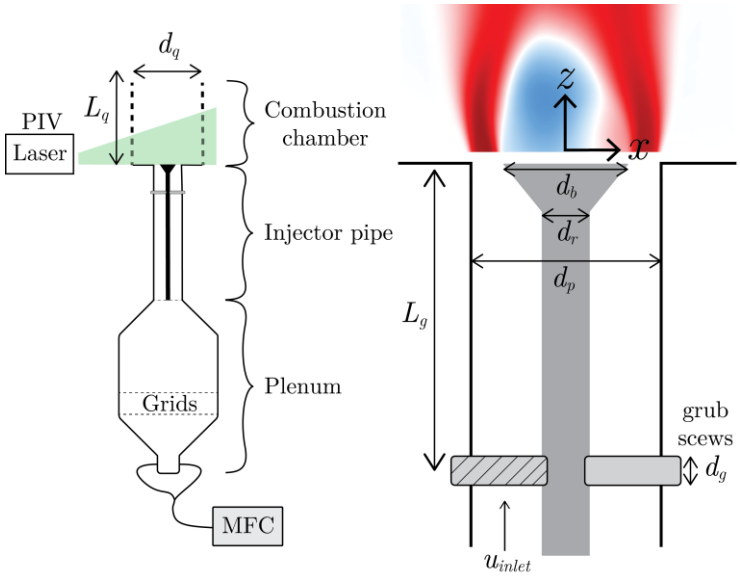

Fig. 5 Single sector atmospheric test rig schematical view.

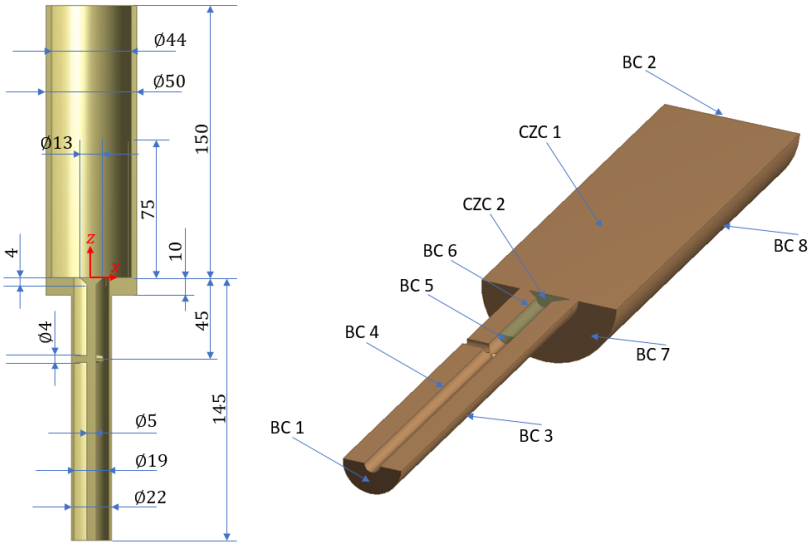

Fig. 6 Measurements (in mm) of burner CAD geometry and boundary names of computational domain.

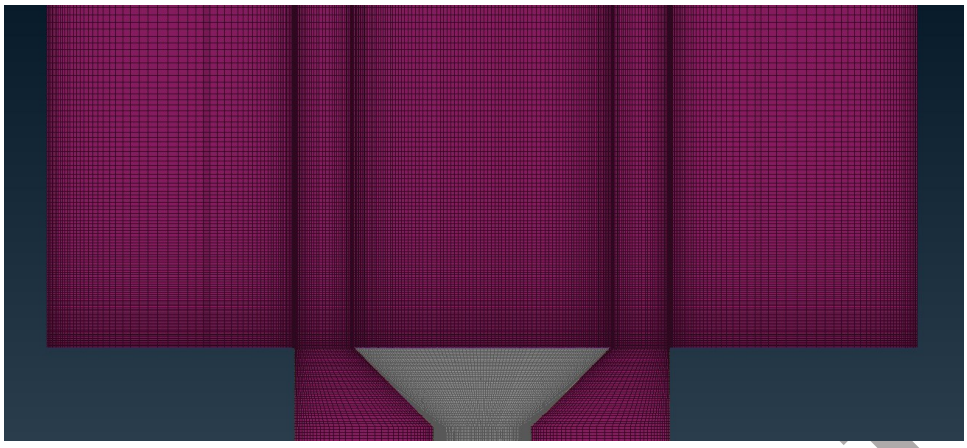

730
731 Fig. 7 Computational grid section view.
732

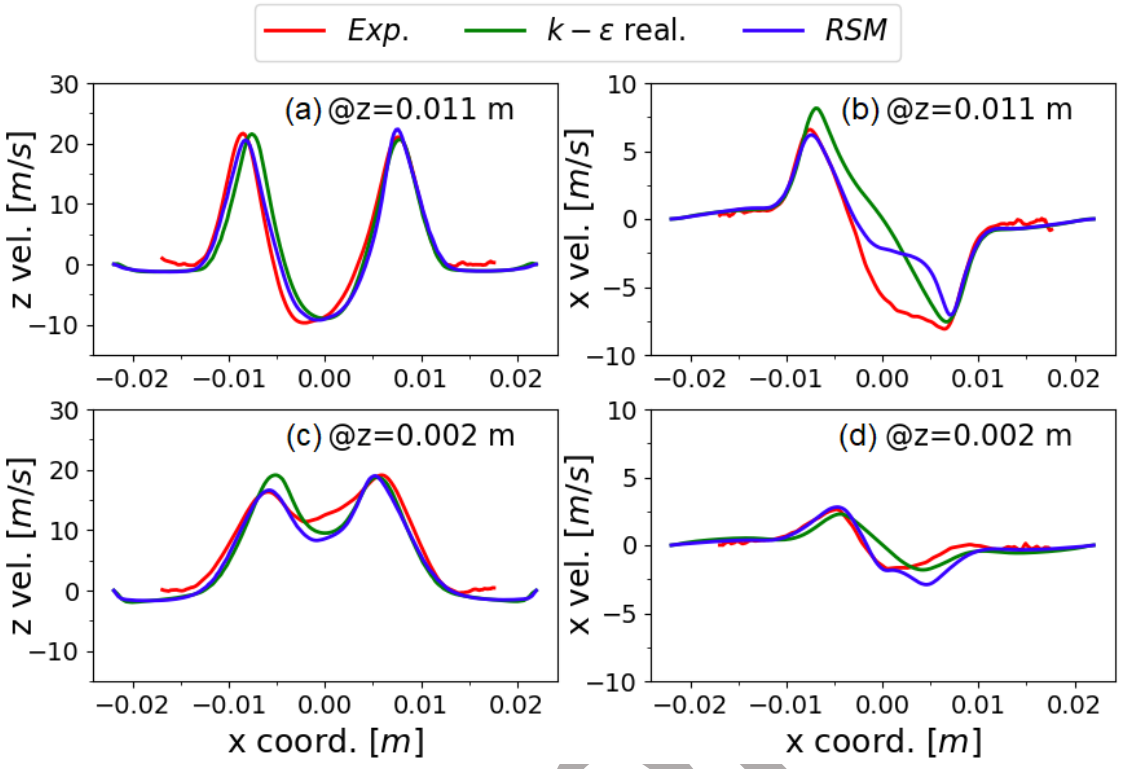

Fig. 8 Cold-flow z (axial) and x (transversal) velocities at different axial positions with different turbulence models ($u_{inlet} = 11.8\ m/s$).

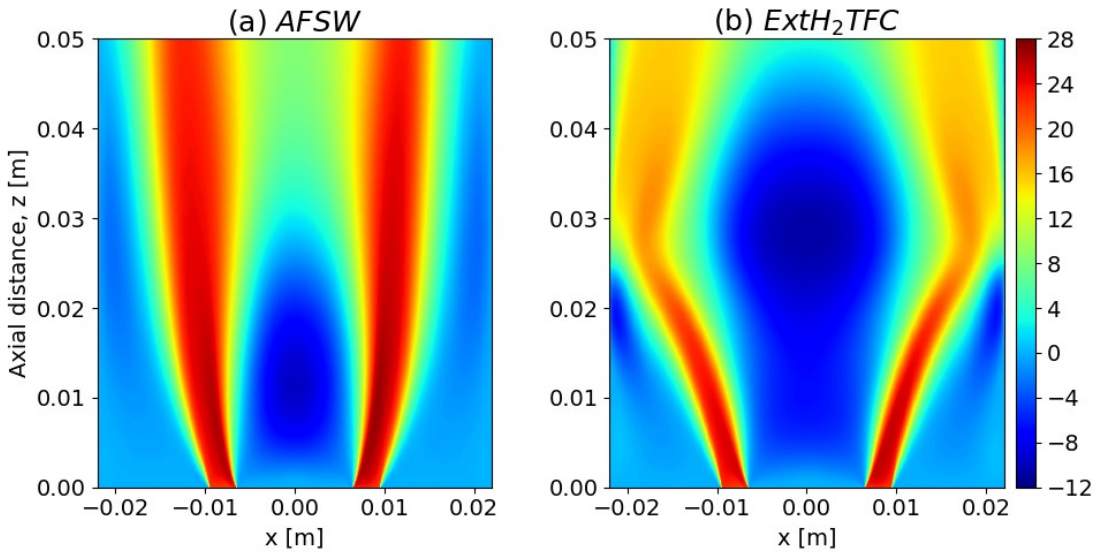

737
738 Fig. 9 Axial velocity for (a) AFSW and (b) ExtH_2TFC with 0% H_2 reacting flow.
739

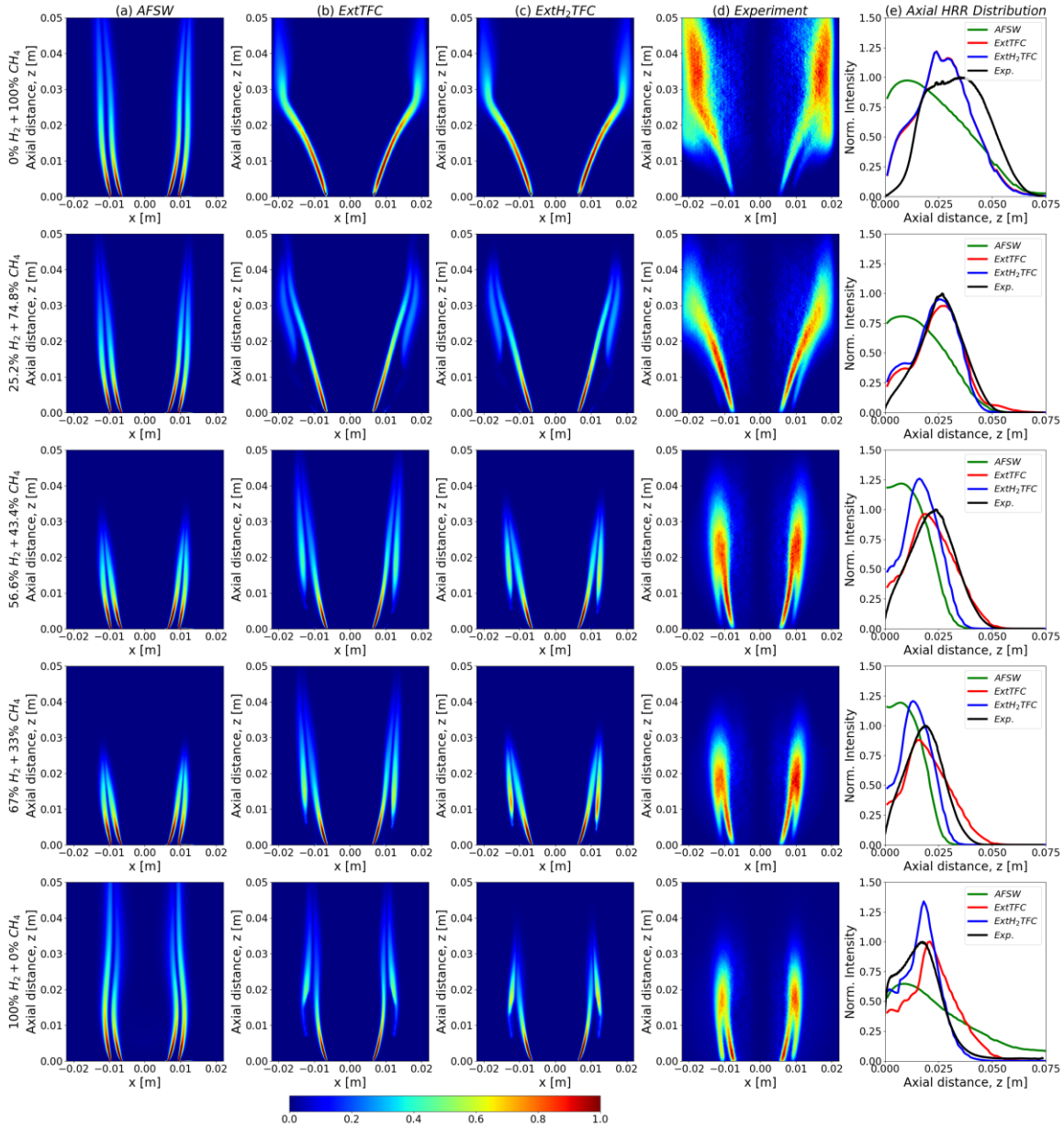

Fig. 10 Heat release rate distributions from 3 different turbulent flame speed models: (a) AFSW, (b) ExtTFC, (c) ExtH_2TFC and (d) Abel deconvoluted OH^* chemiluminescence images from experiments. (e) Normalized axial heat release distributions are shown in the right column. values are normalized with the maximum local intensity.

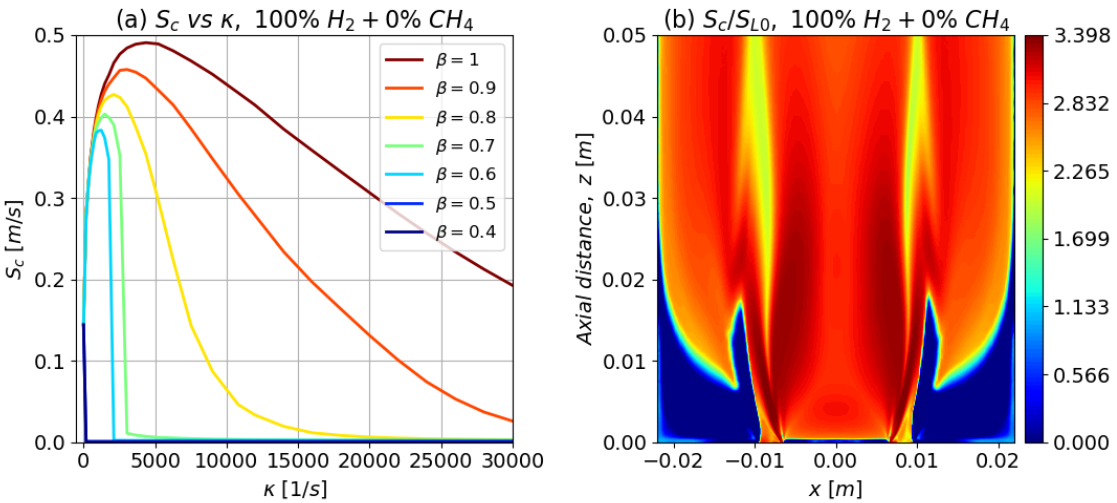

Fig. 11 (a) Laminar consumption speed $S_c(\kappa, \beta)$ as function of flame stretch κ and heat loss coefficient β, (b) ratio of consumption speed $S_c(\kappa, \beta)$ to unstretched laminar flame speed S_{L0} contours (from ExtH_2TFC model) for 100% H_2 + 0% CH_4 CFD case.

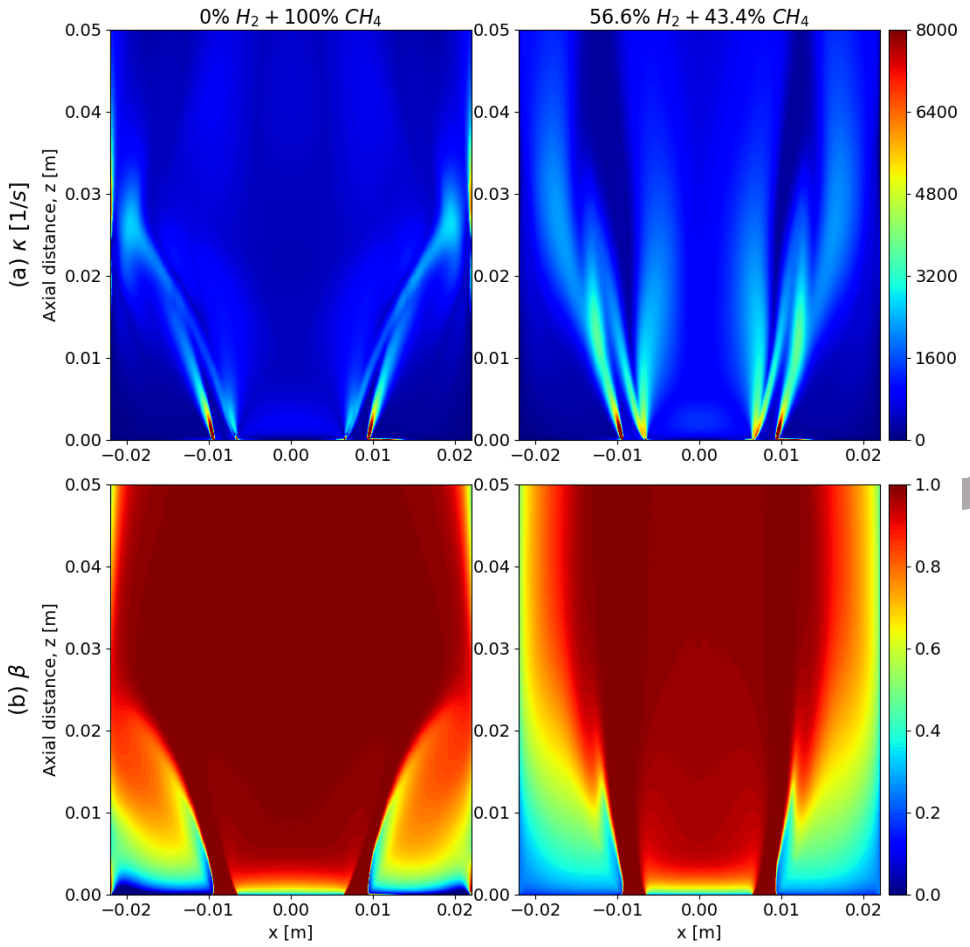

Fig. 12 (a) Total stretch κ, (b) heat loss coefficient β contours from the case with 0% and 56.6% H_2 contents (obtained with ExtH_2TFC model).